

ARTICLE

<https://doi.org/10.1038/s42005-019-0207-8>

OPEN

Spin-driven electrical power generation at room temperature

K. Katcko¹, E. Urbain¹, B. Taudul¹, F. Schleicher^{1,2}, J. Arabski¹, E. Beaurepaire^{1,5}, B. Vilen³, D. Spor¹, W. Weber¹, D. Lacour², S. Boukari¹, M. Hehn², M. Alouani¹, J. Fransson⁴ & M. Bowen¹

On-going research is exploring novel energy concepts ranging from classical to quantum thermodynamics. Ferromagnets carry substantial built-in energy due to ordered electron spins. Here, we propose to generate electrical power at room temperature by utilizing this magnetic energy to harvest thermal fluctuations on paramagnetic centers using spintronics. Our spin engine rectifies current fluctuations across the paramagnetic centers' spin states by utilizing so-called 'spinterfaces' with high spin polarization. Analytical and ab-initio theories suggest that experimental data at room temperature from a single MgO magnetic tunnel junction (MTJ) be linked to this spin engine. Device downscaling, other spintronic solutions to select a transport spin channel, and dual oxide/organic materials tracks to introduce paramagnetic centers into the tunnel barrier, widen opportunities for routine device reproduction. At present MgO MTJ densities in next-generation memories, this spin engine could lead to 'always-on' areal power densities that are highly competitive relative to other energy harvesting strategies.

¹Institut de Physique et Chimie des Matériaux de Strasbourg, UMR 7504 CNRS, Université de Strasbourg, 23 Rue du Loess, BP 43, 67034 Strasbourg, France.

²Institut Jean Lamour UMR 7198 CNRS, Université de Lorraine, BP 70239, 54506 Vandœuvre les Nancy, France. ³Institut de Chimie, UMR 7177 CNRS, Université de Strasbourg, 4 Rue Blaise Pascal, CS 90032, 67081 Strasbourg, France. ⁴Department of Physics and Astronomy, Uppsala University, Box 516, 75120 Uppsala, Sweden. ⁵Deceased: E. Beaurepaire. Correspondence and requests for materials should be addressed to M.B. (email: bowen@unistra.fr)

A solar cell's electronic potential landscape is crafted such that, when a photon is absorbed, the resulting electron and hole (the absence of an electron) flow in opposite directions. Since they carry an electrical charge of opposite sign, this generates an electrical current. Two low-temperature experiments^{1,2} have suggested that, by astutely designing the magnetic potential landscape of a quantum dot (QD) device, electrons with a spin \uparrow or \downarrow quantum property can flow in opposite directions. This can generate electrical power if the spin \uparrow and \downarrow current channels are imbalanced, i.e. if the overall current is spin-polarized. This apparent current imbalance, and the presence of QDs in both systems, are reminiscent of quantum thermodynamical experiments on single electron boxes, which have demonstrated how to harvest thermal fluctuations^{3,4} and information⁵ to perform work at very low temperatures. These heat and information engines are driven by fluctuation-induced quantum tunneling on/off of QDs, with a transmission asymmetry between left and right leads that can be energy-dependent due to the QD's discrete energy levels^{6,7}. A few reports have theoretically⁸ and experimentally (using nitrogen vacancies in diamond⁹) taken into account the electron spin.

Inspired by the report of Miao et al.², and by recent progress in quantum thermodynamics^{3–12}, we propose that a spin-split paramagnetic (PM) quantum object can enable electrons with a spin \uparrow or \downarrow quantum property to flow in opposite directions if the transmission rates on either side of the PM center are spin-dependent. Differing amplitudes in these transport spin channels generate a spontaneous current flow. Measurements across a single MgO magnetic tunnel junction, backed by analytical and ab-initio theories, indicate that this spin engine can operate at room temperature. We discuss strategies to achieve routine device reproduction. Our work also confirms the high transport spin polarization at room temperature of the ferromagnetic metal/molecule interface¹³ inferred from spectroscopy measurements¹⁴.

Results

Figure 1a illustrates our spin engine in the simplified case of a PM center, characterized by two effectively spin-split energy levels. To achieve a strongly spin-dependent transmission rate Γ , the PM center is placed between spintronic selectors—materials systems that ideally favor only one transport spin channel while blocking the other. Examples include half metals^{15–17}, 2D materials with half-metallic properties¹⁸, a normal metal / ferromagnetic tunnel barrier¹⁹ bilayer, and the ferromagnetic metal/molecule interface¹³, also called a ‘spinterface’. The Fe/MgO system may also constitute a spintronic selector given either a sufficient MgO thickness²⁰ and/or the presence of oxygen vacancies^{21–24}. A standard ferromagnetic metal (FM) would also work, albeit with reduced efficiency. Due to this combination of spintronic selectors and spin-split PM states, a spin $\uparrow(\downarrow)$ electron may only depart the PM toward the left(right) electrode at the energy of the PM center's corresponding spin state.

Hai et al.¹ used a MnAs ferromagnetic metal with a conventional ($\sim 50\%$) spin polarization of conduction states, and applied a magnetic field to spin-split their MnAs QDs and obtain power generation at 3K. It is unclear whether this experiment could have worked at higher temperatures. Miao et al.² filtered the electron spin upon transport across EuS ferromagnetic tunnel barriers at 1K, i.e. below its ordering temperature $T_C \sim 16.8$ K. Here, spin splitting of the Al QD is induced by electronic coupling to one EuS barrier.

Reports indicate that several spintronic selector tracks include materials science candidates (e.g. the Fe/MgO MTJ class^{20,22}, the half-metallic Co_2FeAl ¹⁷ or the ferromagnetic tunnel barrier CoFe_2O_4 ¹⁹) that can operate at/beyond room temperature (RT).

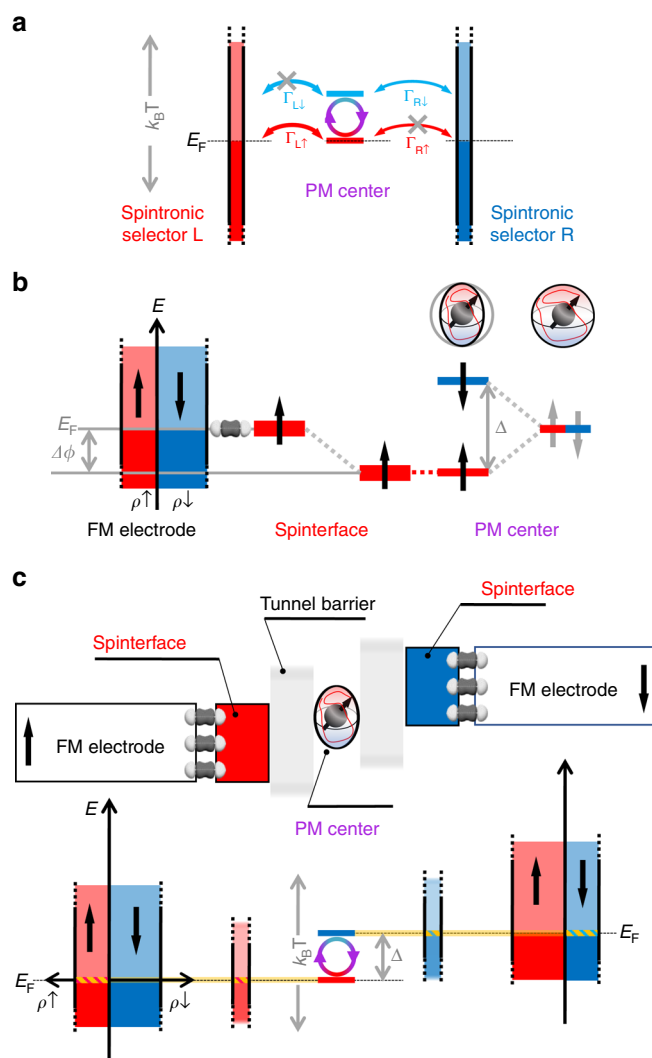


Fig. 1 A room-temperature spin engine. **a** Illustration of asymmetries in the spin-induced transmission rates Γ across a single paramagnetic (PM) center between spintronic selectors L and R. Spinterfaces^{13,14,25,26}, half-metals^{15,17}, Fe/MgO MTJs^{20,22}, and ferromagnetic tunnel barriers¹⁹ can fulfill the role of a spintronic selector. **b** Spin-conserved quantum tunneling between a spinterface and a PM center deforms the PM center's Bloch sphere, thereby splitting^{27,28} its spin states by Δ , and shifts the spinterface's Fermi level (E_F) by $\Delta\phi$. **c** The spintronic landscape across a magnetic tunnel junction, comprising spinterfaces and a PM center, in its antiparallel (AP) magnetic state exhibits a spontaneous bias voltage $\Delta V \leq \Delta$. A yellow band designates the thermally rectified, spin-polarized current involving striped segments of the ferromagnet (FM) and spinterface density of states. The spin engine generates work by harvesting thermal spin fluctuations ($k_B T$) on the PM center. See text for details. In all panels, red (blue) correspond to spin $\uparrow(\downarrow)$ states

To obtain RT electrical generation, and in the process demonstrate it to be a RT spintronic selector, we utilize the spinterface^{13,14,25,26}. This refers to a low energy bandwidth, low density of highly spin-polarized states that arise at room temperature from spin-polarized hybridization between the highly degenerate electronic states of a FM metal such as Co and the few, energetically discrete states of molecules, including carbon atoms²⁶. The spinterface is weakly conducting, and its magnetic orientation naturally follows that of the FM metal. To date, only spin-polarized photoemission spectroscopy^{14,26} suggests that the spinterface may be a spintronic selector at RT.

We now utilize the case of the spinterface to illustrate several key considerations of how spintronic selectors and PM centers can interact to form the spin engine's transport path. Upon connecting the spinterface to the PM state (see Fig. 1a), spin-conserved quantum tunneling conditions the resulting spin-polarized landscape in the following significant ways. First, the spinterface's density of states (DOS) with a spatially oriented spin polarization generates a corresponding spintronic anisotropy in the PM state's stochastic spin distribution^{27,28}, thereby deforming the PM's Bloch sphere of spin states. This generates an energy difference Δ between the PM center's spin states and increases the probability that an electron tunnel onto/off of the PM if its spin is aligned to the spinterface's spin referential (see Fig. 1b). The ensuing preferential charge flow for that spin channel effectively shifts² the spinterface/FM metal's Fermi level by $\Delta\phi$ toward that spin state of the PM center. We are thus describing how the spinterface can modify a metal's properties²⁹, namely its Fermi level position, through an additional mechanism.

In a perfectly symmetric magnetic tunnel junction (MTJ) that implements spin-conserved tunneling between these two key ingredients—spinterfaces and a PM site—no net current (I) should flow in the MTJ's parallel (P) orientation of electrode magnetizations. However, in the MTJ's antiparallel (AP) magnetic state (see Fig. 1a), the two FM electrode Fermi levels are shifted away from one another, each toward the corresponding spinterface-selected spin state of the PM center. The resulting spontaneous bias voltage ΔV between the FM electrodes thus scales with the amplitude of the spinterface's spin polarization and the energy difference Δ between the PM center's spin \uparrow and \downarrow states. Since an experimental MTJ cannot be exactly symmetric, one may also anticipate a spontaneous bias, or current, in the MTJ's P state, albeit of lower amplitude.

To generate work, the spin engine harvests energy from the spin fluctuations that are thermally induced on the PM center. This thermal spin state mixing on the PM center enables current to flow from one spinterface to the other, even against the built-in ΔV in the MTJ's AP magnetic state. The spin engine thus requires that $\Delta \leq k_B T$, and thus a balance between the tunneling-induced energy shift $\Delta\phi$ of the spinterface state to the PM center's spin state and thermal fluctuations, as weighed by the spinterface's spin polarization (see Fig. 1c). This thermal energy harvesting can be expected to cool the PM center. Furthermore, the fully spin-polarized current flowing across the spinterface perturbs the FM ground state of the electrode through a spin accumulation-induced interfacial resistance³⁰. The resulting heat generation in the FM electrode must be dissipated for our spin engine to work. Finally, the spinterface's low density of highly spin-polarized states may be beneficial to RT operation. Indeed, it protects the energetically discrete PM spin states against thermal broadening from the FM electrodes. As discussed theoretically in Supplementary Notes 1 and 2, the thermal fluctuations in current are rectified first upon transport from the FM electrode onto the spinterface, and furthermore upon transport from the spinterface onto the PM center's spin state. This, along with the spinterface's high spin polarization, strongly dampens any energy smearing of the PM center's discrete spin states. The resulting energetically sharp, spin-polarized effective current path involving the striped DOS of the FM electrodes and spinterfaces is schematized in Fig. 1c by the yellow band.

With the support of analytical and ab-initio theories, we believe to have observed an experimental realization of this spin engine through measurements across a single MgO MTJ at room temperature (RT; see junction statistics in Supplementary Note 3). As described hereafter, this MTJ integrates Co/C spinterfaces with nearly total spin polarization²⁶, and paramagnetic C atoms³¹ on the oxygen vacancy sites of the MgO tunnel barrier. Referring to

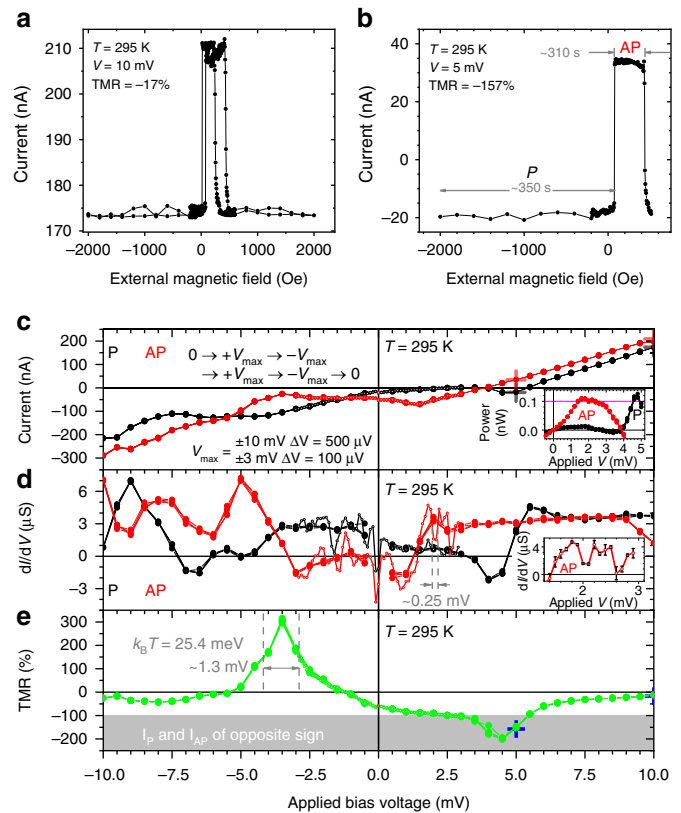


Fig. 2 Spintronics-driven power generation at room temperature. **a**, **b** Magnetic field dependence of current I (H) at **a** +10 mV and **b** +5 mV measured on the 20 μm -diameter magnetic tunnel junction (MTJ). **c–e** Bias dependence of **c** current and **d** numerically derived conductance dI/dV in the MTJ's parallel (P; black; $H = -2000$ Oe) and antiparallel (AP; red; $H = 250$ Oe) states, and **e** the inferred tunneling magnetoresistance (TMR) bias dependence. Two sets of $0 \rightarrow +V_{\text{max}} \rightarrow -V_{\text{max}} \rightarrow +V_{\text{max}} \rightarrow -V_{\text{max}} \rightarrow 0$ sweeps spanning ± 10 mV (± 3 mV) with 500 μV (100 μV) steps are shown. Discrete $I(V)$ points obtained from the $I(H)$ data of **a** and **b** are represented using semi-transparent crosses. TMR data $< -100\%$ (within the gray zone of **c**; see **b**) is achieved when I_P and I_{AP} are of opposite sign at constant V . A non-zero current that depends on the MTJ's magnetic state is observed for $V = 0$. Despite the ~ 50 meV expected thermal smearing for this 295 K measurement, the $+300\%$ TMR peak has a full-width-at-half-maximum of ~ 1.3 meV and statistically relevant conductance oscillations with a ~ 0.25 meV width are observed (see **d** inset). The inset to **d** shows the mean conductance over 4 bias voltage sweeps and the resulting standard deviation as error bars. This spectral sharpness is a direct signature of the spin engine. The inset to **c** shows how the bias-dependent output power depends on the MTJ's magnetic state and can exceed 0.1 nW at room temperature

Fig. 2a, we observe a negative tunneling magnetoresistance ratio, i.e. $\text{TMR} = I_P/I_{AP} - 1 < 0$, at $V = +10$ mV and $T = 295$ K through P/AP magnetic states that are well controlled thanks to an IrMn pinning layer (see Methods). Figure 2b shows the $I(H)$ data acquired at $V = +5$ mV. Over the ~ 350 s needed to ramp H down from -2000 Oe to ~ 0 Oe, the MTJ remains in a P magnetic state, with $I_P < 0$ despite $V > 0$. In the MTJ's AP state, $I_{AP} > 0$ over ~ 310 s. The abrupt magnetic field dependence of the switch in sign of current clearly shows that the current sign change originates from the change in the MTJ's magnetic state, and not the magnetic field amplitude/sweep. Both I_P and I_{AP} exceed the maximum 500 pA possible experimental offset by nearly 2 orders of magnitude (see Supplementary Notes 4 and 5). Thus, in this

MTJ, the direction of static current flow can be reversed by simply switching the MTJ's spintronic state.

Since the external magnetic field is static, and we do not expect a spin texture in our FM electrodes, a spin motive force explanation^{1,32,33} seems unlikely. In these and our experiments, no explicit temperature difference between electrodes, or temperature gradient, is applied to the device, such that a spin caloritronics³⁴ explanation, while possible, is not obvious. We further discuss in the Methods and Supplementary Note 5 how photovoltage/photocurrent and conventional/spintronic thermovoltage^{17,35} artifacts can be excluded here.

These I(H) datapoints are confirmed through I(V) measurements at RT in the MTJ's P and AP states (see Fig. 2c), which reveal the following features: (1) at $V = 0$, $I_P \neq I_{AP} \neq 0$, with an amplitude that also exceeds any experimental offset by nearly 2 orders of magnitude; (2) a non-zero applied bias V leading to a measured $I = 0$ whose amplitude depends on the MTJ's magnetic state; (3) power generation above 0.1 nW whose bias dependence depends on the MTJ's magnetic state, with a maximum current $I_{AP} \approx -70$ nA at $V = +1.4$ mV (see panel (c) inset using data from Supplementary Fig. 5a; (4) bias-driven oscillations in current that depend on the MTJ's P/AP magnetic state, and thus on spin-dependent transport; (5) a bias range for which I_P and I_{AP} are of opposite sign, leading to $\text{TMR} < -100\%$. These features of the $0 \rightarrow +V_{\text{max}} \rightarrow -V_{\text{max}} \rightarrow +V_{\text{max}} \rightarrow -V_{\text{max}} \rightarrow 0$ I(V) sweep are reproduced with high fidelity in Fig. 2c for another such sweep with differing maximum applied bias V_{max} and bias step (i.e. a differing effective bias sweep rate), as well as by additional datasets (see Supplementary Note 4). This eliminates any junction instability/memristive/Joule heating explanation³⁶. (6) The numerically derived junction conductance dI/dV of the data of Fig. 2c, shown in Fig. 2d, reveals spintronically determined conductance jumps, and spectral features as low as 0.25 meV—despite the $2k_B T \approx 50$ meV thermal smearing expected at 295 K—that are statistically beyond the error bar (see Fig. 2d inset and Supplementary Note 6 for full dataset and error bars) thanks to an excellent signal-to-noise ratio.

This spectral sharpness is also witnessed through a 300% TMR peak with a full-width-half-max of ~ 1.3 meV (see Fig. 2e), which arises from a combination of local maxima(minima) in $I_P(I_{AP})$ at $V = -3.5$ mV. This non-optimized device's spintronic performance at 295 K rivals the 600% record for FeCoB/MgO-class MTJs—obtained through a 20-fold performance increase over 7 years^{37,38}—but since the Co electrodes cannot be *bcc*-oriented here^{20,39} (see Methods), this spintronic performance cannot arise from symmetry filtering. Within a simple Jullière model²⁰ interpretation of the TMR amplitude, and from our analytical theory presented hereafter, this can be ascribed in part to the high transport spin polarization of the Co/C spinterface²⁶ at RT.

This spectral sharpness in magnetotransport features at RT despite the expected thermal broadening, and the excellent signal-to-noise ratio, can be interpreted as an experimental signature of our spin engine at work. Indeed, according to quantum thermodynamics^{4,7}, the harvesting of spin fluctuations on the PM centers is expected to lower their temperature. From $k_B T \approx 0.25$ meV, we estimate an effective electronic temperature of the PM centers of 3 K. This cooling is the manifestation of harvesting energy from the PM centers' spin fluctuations upon spin rectification in the junction.

Since a non-zero current is present at $V = 0$ across this normally passive component, we observe that the MTJ is intrinsically out of equilibrium. Consequently, to further link our experimental results with our conceptual spin engine, we analytically consider an out-of-equilibrium nanotransport path across the MTJ comprising two PM centers (see Fig. 3a and the Methods/Supplementary Note 1 for details). Their initially discrete energy

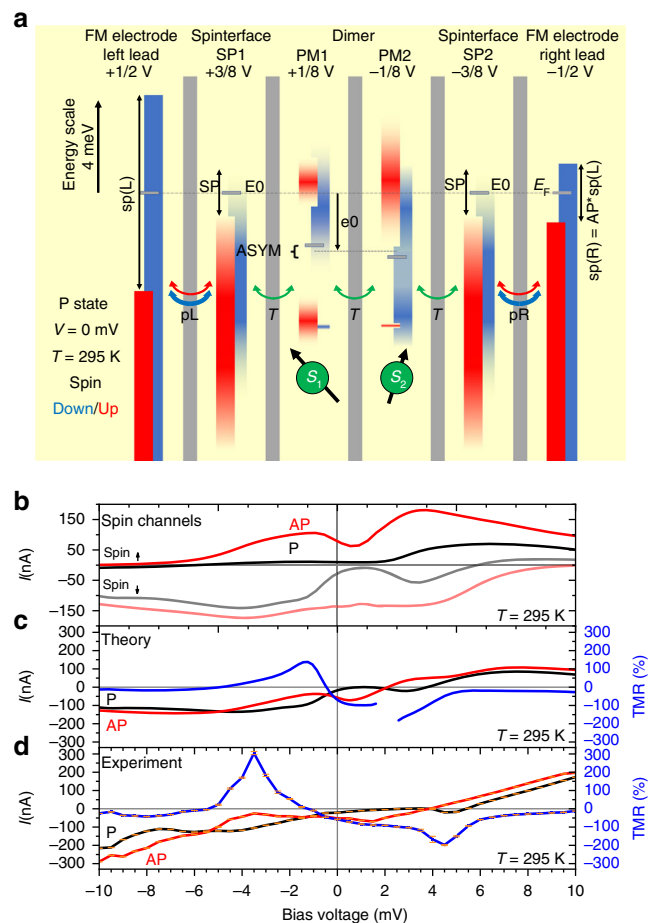


Fig. 3 Analytical theory linking experiments to the spin engine. **a** Schematic of the analytical model of spin-conserved transport across a paramagnetic dimer (PM1 & PM2 centers) separated from each ferromagnetic (FM) lead by a spinterface. The calculated case of the P magnetic state at $V = 0$ is shown. **b** Theoretical bias dependence of spin \uparrow (solid) and spin \downarrow (semi-transparent) current in the magnetic tunnel junction's parallel (P; black) and antiparallel (AP; red) magnetic states. **c** Theoretical and **d** averaged experimental bias dependencies of current in the MTJ's P (black) and AP (red) magnetic states, and of the resulting tunneling magnetoresistance (TMR; green), using the same current/TMR scales. Experimental standard deviations are shown as error bars in orange. Within an apparent factor in the voltage scale, the analytical model including the out-of-equilibrium hypothesis strongly mimics the room-temperature (RT) experiment, thereby linking it to the spin engine

levels (gray lines) are broadened to form a PM dimer as bonding/anti-bonding and spin degeneracies are lifted (see PM 1&2 of Fig. 3a) through a magnetic exchange coupling that is bias-dependent^{28,40}. To place the junction out of equilibrium, we impose a spin splitting of the FM electrodes' chemical potential. Following our spin engine proposal, our analytical model's magnetic interactions (with Heisenberg, Ising and Dzyaloshinskii-Moriya contributions) result in a spintronic anisotropy^{27,28} onto PM1 and PM2 due to the spatially oriented, spin-polarized DOS of each FM electrode, as mediated by spinterfaces (SP1 & SP2).

Consistently with our experimental results, we constrain the model's 7-fold fitting parameter space using the following physical requirements: 1) the parameters should realistically describe the MTJ's outer properties (FM electrode + spinterface), including a higher spin polarization at the lower Co/MgO MTJ interface due to C dusting²⁶ (see Methods); 2) these outer properties

should remain identical in the MTJ's P/AP magnetic states; 3) only minor changes to the PM dimer's properties are allowed between the P and AP cases. To account for $T = 295$ K, the FM electrodes' Fermi level is broadened by 26 meV (not shown in Fig. 3a). Results of this analytical model shown in Fig. 3b, c were acquired using a same set of parameters (see Methods for details) for the MTJ's P/AP outer properties: $sp = 8.4$, $SP = 2$, $pL = pR = 0.35$, $AP = 0.3$, $E_0 = 0$, with pR and AP changing sign upon $P \leftrightarrow AP$, while we introduced minor variations in the PM dimer's starting conditions for P(AP): $e_0 = -2.5(+0.85)$ and $ASYM = 0.5$ (-0.75). Parameters are described in the Methods. Supplementary Fig. 2 shows the complex bias dependence of this spintronic potential landscape for each spinterface/PM center (SP1, PM1, PM2 & SP2), depending on the spin channel and the MTJ's P or AP magnetic state considered. Note how our model fulfills the spin engine's $\Delta < k_B T$ condition.

Referring to Fig. 3b, we observe a bias anti-symmetric imbalance in the oppositely propagating spin channels of current, which strongly depends on the MTJ's P/AP magnetic state. This leads to a sizeable spintronic difference in current, in particular at $V = 0$. We recopy the $I_P(V)$, $I_{AP}(V)$ and $TMR(V)$ experimental data of Fig. 2c/e as Fig. 3d in order to compare them with their analytical counterparts, shown in Fig. 3c. Despite a skewed bias position that could underscore the simplicity of the bias voltage distribution (see Fig. 3a), our out-of-equilibrium analytical model reproduces all trends and salient features of the experimental magnetotransport data. This includes the spintronically dependent non-zero current at $V = 0$, large TMR peak at $V < 0$ and the bias region for $V > 0$ with differing signs of I_P and I_{AP} . A degraded agreement at large V likely reflects how our model only considers sequential transport across the 4 QDs, and not direct transport between the FM electrodes, which can become significant as the QD levels are energetically shifted away from one another. This agreement between theory and experiment compares quite favorably with respect to the state of the art^{21,22,41,42}.

In general, compared to low-temperature transport across well-characterized quantum objects (e.g. from single atoms and dimers to molecules and atomic clusters^{43–49}) thanks to a scanning tunneling microscope (STM), it is thus far difficult to assemble and ascertain the effective nanotransport path⁵⁰ in a solid state device, especially for the oxides used as MTJ barriers. Here, uncontrolled imperfections such as oxygen vacancies in the MgO tunnel barrier can concentrate electronic tunneling transport across a macrojunction onto a nanotransport path^{50,51}, such that the device operates due to a rare tunneling event⁵². This is what enables⁵³ the spin transfer torque effect underscoring key MTJ-based technologies^{54,55}. As detailed in Supplementary Notes 7 and 8, while descriptions of the PM dimer in terms of Mn atoms or oxygen vacancies are much less likely here, paramagnetic C atoms occupying oxygen vacancy sites in MgO are possible considering our MTJ stack with C-dusted MgO interfaces. Indeed, carbon capture by single/double oxygen vacancies, which are present in our MgO^{21,23,53}, is energetically favorable (see Supplementary Note 7 and the work of Tiusan et al.⁵⁶) and can yield both paramagnetic monomers (see Supplementary Note 7) and dimers³¹.

Our ab-initio theory shows that the C–C distance is crucial in order to reproduce our analytical model's results: only in a 4th nearest-neighbor positioning does the C dimer simultaneously exhibit AF coupling (favorable over FM by 0.125 eV, i.e. above experimental $k_B T$) and generate four states around the Fermi level E_F of a Co/MgO/Co MTJ (see Fig. 4 and Supplementary Note 9). On the other hand, C pairs in 1st, 2nd, 3rd, and 5th nearest-neighbor configuration generate a FM state (see Supplementary Note 7), which would be inconsistent with our analytical model. This stringent C impurity positional requirement on the oxygen

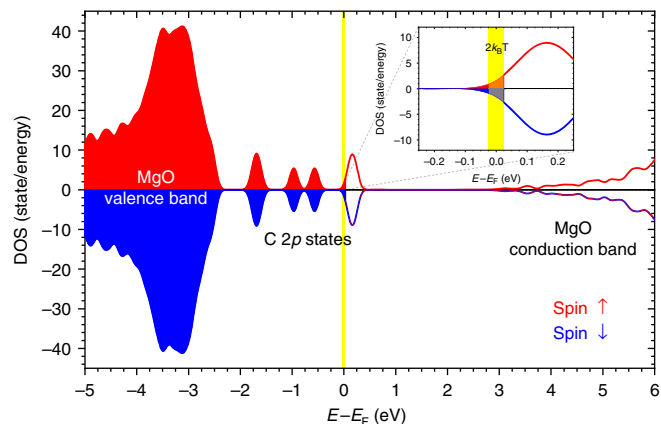


Fig. 4 Origin of the experiment's paramagnetic centers. Ab-initio calculations of the spin-resolved density of states (DOS) of MgO containing a carbon dimer in 4th nearest-neighbor configuration. The paramagnetic, antiferromagnetically coupled C dimer generates energy levels around the magnetic tunnel junction's Fermi level E_F , including four spin-degenerate states that intersect E_F , thereby reproducing the analytical model's description of PM centers 1 and 2. See Supplementary Note 9 for the determination of the MTJ's E_F energy position

sublattice might explain why our spin engine was experimentally observed only once out of ~ 200 attempts (see Supplementary Note 3).

Discussion

To achieve routine experimental reproducibility, we propose that all spintronic selector tracks be attempted (see introduction), noting that, in addition to the two published reports^{1,2}, similar effects were observed at low temperature on MTJs with manganese half metals⁵⁷. In all cases, control over the spatial position and density of the barrier's PM centers will be required with a precision that, at this time, remains the domain of model STM-assembled junctions^{43–49}. Considering that all reports involved microscale devices, this suggests reducing the junction's lateral size from the micro- to the nano-scale. In an oxide track, one may study tunnel barriers in which an oxygen vacancy-rich central region—achieved e.g. by varying oxygen concentration in an Ar sputtering plasma during growth⁵¹, is nominally seeded with impurities to be trapped by these vacancies as PM centers. Control over the electronic properties of, and magnetic interactions⁵⁸ between, PM centers in molecules suggests another, organic-based track using spintronic nanojunctions^{59,60}. Whatever the route, except for an AF-coupled PM dimer, the PM center(s) should experience dominant tunneling from one spintronic selector in order to adopt that selector's spin referential (see Fig. 1b and discussion). This can arise by tuning the selector/PM center tunneling rate through the insertion of an oxide/organic interlayer. Cleverly crafted operando techniques⁵⁰ that can directly characterize the PM center's properties within the device's nanotransport path can boost research efficiency. Overall, MgO spintronics represents a compelling route. Indeed, it benefits from both industrial penetration^{54,61} and knowledge on how oxygen vacancies craft the spintronic nanotransport path^{21–24,53}, boasts lateral sizes down to 4.3 nm⁶², and has been conjugated with half-metallic electrodes operating at RT¹⁷. PM centers can be formed in MgO by trapping C, N or Si on oxygen vacancies (see Fig. 4, the work of Wu et al.³¹ and Supplementary Note 7).

To complement this heat description of our work, we briefly note in the Supplementary Note 10 that the rectification of

thermal fluctuations, which are present experimentally and analytically, can generate work when combined with an increase in the entropy of quantum information¹¹ arising from spin transport onto the PM center due to its spin fluctuations. A quantum thermodynamical theory along a similar spintronic path has been proposed⁸, while classical electronic implementations using capacitively coupled quantum dots have been demonstrated at low temperature^{3,5,63}. Our results should thus generate research initiatives on quantum electronic circuits at the rather unexplored intersection between quantum thermodynamics^{3–12} and spintronics^{20,34,54}. More generally, our work also indicates that the high transport spin polarization, and low density of states, of spinterfaces represent a compelling approach to integrating the quantum properties of nano-objects within a solid-state device's operation at room temperature, beyond proof-of-concept electronic decoupling strategies^{43,64}.

The MTJ used to demonstrate our spin engine is an industrial-grade microelectronic device class used as the read head of hard disk drives, and with promising potential toward low-power information storage⁵⁴ and bio-inspired computing⁵⁵. If routine reproducibility can be achieved, then for a typical STT-MRAM⁶¹ 2D array of 50 nm-wide MTJs with a pitch of 90 nm, assuming that the 0.1nW occurred through a single conduction channel, the resulting power density would be substantial. As an example, a suitable series/parallel assembly on a 1 cm² chip could deliver ~29.4 W of power to a 0.1 Ω load at 3.5 V. See Supplementary Note 11 for more details. Even considering 1% efficiency due to engineering issues (e.g. managing heat flow, interconnect resistances...), this power density would still exceed the raw solar power density on the earth surface by a factor of three. Further research may see the MTJ play a key role not only in information & communication, but also renewable energy, technologies.

Methods

Device preparation and batch characterization. Ta(5)/Co(10)/IrMn(7.5)/Co(4)/C($d_1 = 0, 0.3, 0.6, 0.9$)/MgO(2.5 nm)/C($d_2 = 0, 0.3, 0.6$)/Co(10)/Pt(4) samples (all thicknesses in nm) were sputter-grown on Corning 1737 glass substrates⁶⁵. Stacks were post-annealed in an in-plane magnetic field of 200 Oe for 1 h at a temperature T_a of 200 °C to magnetically pin the lower electrode thanks to the IrMn antiferromagnetic layer. This low annealing temperature precludes the diffusion of Mn into the barrier⁶⁶, though it can promote C diffusion into MgO⁶⁶. Samples were then processed by optical lithography⁶⁷ into 20 μm-diameter MTJs, and measured on a variable-temperature magnetotransport bench. Within the study, 216 MTJs that exhibited neither a short-circuit nor an open circuit had a median $R = 4395 \Omega$ in the MTJ's P state, i.e. a median R.A. product of $1.38E6 \Omega \cdot \mu m^2$. Only 1 out of 168 20 μm-diameter MTJs tested at $T = 295 K$, with $d_1 = 0.9$ and $d_2 = 0$, a ten-fold larger RA product ($R = 57.7 k\Omega$, R.A. = $1.81E7 \Omega \cdot \mu m^2$; standard contact resistances) and anomalous $TMR < 0$ at $V = +10$ mV, revealed these peculiar power generation features and high TMR. An additional 48 MTJs did not exhibit $I \neq 0$ at $V = 0$. We presume that annealing-induced C migration into MgO generated the MTJ's spinterfaces and PM centers. The lower R found in passive MTJs suggests the presence of several conduction channels, each with a slightly different nanotransport path, such that electrical generation effects are averaged out.

Possible transport artifacts. Measurements on this MTJ were conducted over 90 min in 4-point measurement mode within a dark cryostat that remained between 295.3 K and 294.5 K with sample heater off. Furthermore, these peculiar transport features strongly depend on the MTJ's P/AP magnetic state. We in particular observe that $I \neq 0$ at $V = 0$. We can therefore exclude thermovoltage photovoltage/photocurrent, as well as any conventional or spintronic thermovoltage explanations. We discuss these discarded artifact sources in more detail in Supplementary Note 5.

Analytical theory. The analytical model^{28,40} symmetrically segments the MTJ's bias drop into 6 zones around the junction mid-point, for which $V \equiv 0$, using the same bias sign convention as in experiment. Current flow across the left-hand (right-hand) FM electrode is modeled by a spin-splitting $sp(sp \times AP)$ of its chemical potential. The DOS of the spinterfaces SP1 & SP2 consists in 10meV-wide bands

that are centered around E_F at $V = 0$ and are spin-split by SP. A constant $E_0 = 0$ was used. PM 1&2 model the paramagnetic dimer as two spin states S_1 and S_2 that, initially, are energetically discrete, are positioned e_0 away from E_F at $V = 0$, and are energy-split by ASYM but are not spin-split. Current flows between the FM electrodes across SP1/PM1/PM2/SP2 through a tunneling rate T , which was fixed at [1 1 1] between SP1/PM1; PM1/PM2; PM2/SP2. Finally, pL(pR) describes a possible spin polarization of the tunnelling transmission between the left(right) FM lead and SP1(SP2). The MTJ's AP state is described by switching the sign of pR and AP, i.e. by flipping the right-hand FM electrode magnetization. This experimentally corresponds to the free Co layer of the top FM electrode. $AP = 0.3$ is consistent with an experimentally larger spin polarization of the C-dusted Co lower FM electrode²⁶, and to $d_1 \neq d_2$. Supplementary Note 1 further details the model's transport formalism.

Ab-initio theory. Within density functional theory, the electronic properties of the C dimer within MgO were computed using 64-atom supercells with a simple cubic structure with two substitutional carbon atoms in various configurations (see Supplementary Note 7 and Supplementary Fig. 8). These calculations were done using VASP code⁶⁸ based on the projector augmented wave (PAW) method⁶⁹ and the Pedrew, Burke, Enzerhof (PBE)⁷⁰ generalized gradient approximation for the exchange-correlation potential. The kinetic energy cutoff value of 500 eV for the plane wave basis set and the convergence criterion for the total energy of 10^{-8} eV is used. The carbon-doped structures are fully relaxed using a conjugate-gradient algorithm, such that the forces acting on atoms be less than 0.001 eV/Å. A k -point mesh of $6 \times 6 \times 6$ with the Methfessel-Paxton method with a smearing $\tau = 0.1$ eV is used. See Supplementary Note 9 for the determination of E_F within a Co/MgO(12 ML, i.e. ~2.5 nm)/Co MTJ.

Data availability

The data that support the findings of this study are available from the corresponding author upon request.

Received: 3 May 2019 Accepted: 1 August 2019

Published online: 25 September 2019

References

- Hai, P. N., Ohya, S., Tanaka, M., Barnes, S. E. & Maekawa, S. Electromotive force and huge magnetoresistance in magnetic tunnel junctions. *Nature* **458**, 489–492 (2009).
- Miao, G.-X., Chang, J., Assaf, B. A., Heiman, D. & Moodera, J. S. Spin regulation in composite spin-filter barrier devices. *Nat. Commun.* **5**, 3682–3687 (2014).
- Thierschmann, H. et al. Three-terminal energy harvester with coupled quantum dots. *Nat. Nanotechnol.* **10**, 854–858 (2015).
- Jalil, G. et al. Experimental realization of a quantum dot energy harvester. *Phys. Rev. Lett.* **123**, 117701 (2019).
- Koski, J. V., Kutvonen, A., Khaymovich, I. M., Ala-Nissila, T. & Pekola, J. P. On-chip Maxwell's demon as an information-powered refrigerator. *Phys. Rev. Lett.* **115**, 260602 (2015).
- Sánchez, R. & Büttiker, M. Optimal energy quanta to current conversion. *Phys. Rev. B* **83**, 085428 (2011).
- Strasberg, P., Schaller, G., Brandes, T. & Esposito, M. Quantum and information thermodynamics: a unifying framework based on repeated interactions. *Phys. Rev. X* **7**, 021003 (2017).
- Ptaszyński, K. Autonomous quantum Maxwell's demon based on two exchange-coupled quantum dots. *Phys. Rev. E* **97**, 012116 (2018).
- Wang, W.-B. et al. Realization of quantum Maxwell's demon with solid-state spins*. *Chin. Phys. Lett.* **35**, 040301 (2018).
- Benenti, G., Casati, G., Saito, K. & Whitney, R. S. Fundamental aspects of steady-state conversion of heat to work at the nanoscale. *Phys. Rep.* **694**, 1–124 (2017).
- Mandal, D. & Jarzynski, C. Work and information processing in a solvable model of Maxwell's demon. *Proc. Natl Acad. Sci. USA* **109**, 11641–11645 (2012).
- Rio, L., del Åberg, J., Renner, R., Dahlsten, O. & Vedral, V. The thermodynamic meaning of negative entropy. *Nature* **474**, 61–63 (2011).
- Delprat, S. et al. Molecular spintronics: the role of spin-dependent hybridization. *J. Phys. Appl. Phys.* **51**, 473001 (2018).
- Djegloul, F. et al. High spin polarization at ferromagnetic metal-organic interfaces: a generic property. *J. Phys. Chem. Lett.* **7**, 2310–2315 (2016).
- Bowen, M. et al. Half-metallicity proven using fully spin-polarized tunnelling. *J. Phys. Condens. Matter* **17**, L407–L409 (2005).

16. Liu, H. et al. Giant tunneling magnetoresistance in epitaxial $\text{Co}_2\text{MnSi}/\text{MgO}/\text{Co}_2\text{MnSi}$ magnetic tunnel junctions by half-metallicity of Co_2MnSi and coherent tunneling. *Appl. Phys. Lett.* **101**, 132418 (2012).
17. Boehnke, A. et al. Large magneto-Seebeck effect in magnetic tunnel junctions with half-metallic Heusler electrodes. *Nat. Commun.* **8**, 1626 (2017).
18. Ashton, M. et al. Two-dimensional intrinsic half-metals with large spin gaps. *Nano Lett.* **17**, 5251–5257 (2017).
19. Miao, G.-X. & Moodera, J. S. Spin manipulation with magnetic semiconductor barriers. *Phys. Chem. Chem. Phys.* **17**, 751–761 (2015).
20. Miao, G.-X., Münzenberg, M. & Moodera, J. S. Tunneling path toward spintronics. *Rep. Prog. Phys.* **74**, 036501–036519 (2011).
21. Schleicher, F. et al. Localized states in advanced dielectrics from the vantage of spin- and symmetry-polarized tunnelling across MgO. *Nat. Commun.* **5**, 4547 (2014).
22. Taudul, B. et al. Tunneling spintronics across MgO driven by double oxygen vacancies. *Adv. Electron. Mater.* **3**, 1600390 (2017).
23. Schleicher, F. et al. Consolidated picture of tunnelling spintronics across oxygen vacancy states in MgO. *J. Phys. Appl. Phys.* **52**, 305302 (2019).
24. Taudul, B., Bowen, M. & Alouani, M. Impact of single and double oxygen vacancies on electronic transport in Fe/MgO/Fe magnetic tunnel junctions. Preprint at: <https://arxiv.org/abs/1904.02554> (2019).
25. Velev, J., Dowben, P., Tsybmal, E., Jenkins, S. & Caruso, A. Interface effects in spin-polarized metal/insulator layered structures. *Surf. Sci. Rep.* **63**, 400–425 (2008).
26. Djeghloul, F. et al. Highly spin-polarized carbon-based spinterfaces. *Carbon* **87**, 269–274 (2015).
27. Misiorny, M., Hell, M. & Wegewijs, M. R. Spintronic magnetic anisotropy. *Nat. Phys.* **9**, 801–805 (2013).
28. Fransson, J., Ren, J. & Zhu, J.-X. Electrical and thermal control of magnetic exchange interactions. *Phys. Rev. Lett.* **113**, 257201 (2014).
29. Cinchetti, M., Dediu, V. A. & Hueso, L. E. Activating the molecular spinterface. *Nat. Mater.* **16**, 507–515 (2017).
30. Valet, T. & Fert, A. Theory of the perpendicular magnetoresistance in magnetic multilayers. *Phys. Rev. B* **48**, 7099 (1993).
31. Wu, H. et al. Magnetism in C- or N-doped MgO and ZnO: a density-functional study of impurity pairs. *Phys. Rev. Lett.* **105**, 267203 (2010).
32. Barnes, S. E. & Maekawa, S. Generalization of Faraday's law to include nonconservative spin forces. *Phys. Rev. Lett.* **98**, 246601 (2007).
33. Tanabe, K. et al. Spin-motive force due to a gyrating magnetic vortex. *Nat. Commun.* **3**, 845–849 (2012).
34. Hoffmann, A. & Bader, S. D. Opportunities at the frontiers of spintronics. *Phys. Rev. Appl.* **4**, 047001 (2015).
35. Jaramillo, J. D. V. & Fransson, J. Charge transport and entropy production rate in magnetically active molecular dimer. *J. Phys. Chem. C* **121**, 27357–27368 (2017).
36. Baeumer, C. et al. Quantifying redox-induced Schottky barrier variations in memristive devices via *in operando* spectromicroscopy with graphene electrodes. *Nat. Commun.* **7**, 12398–12404 (2016).
37. Bowen, M. et al. Large magnetoresistance in Fe/MgO/FeCo(001) epitaxial tunnel junctions on GaAs(001). *Appl. Phys. Lett.* **79**, 1655 (2001).
38. Ikeda, S. et al. Tunnel magnetoresistance of 604% at 300K by suppression of Ta diffusion in CoFeB/MgO/CoFeB pseudo-spin-valves annealed at high temperature. *Appl. Phys. Lett.* **93**, 082508 (2008).
39. Yuasa, S., Fukushima, A., Kubota, H., Suzuki, Y. & Ando, K. Giant tunneling magnetoresistance up to 410% at room temperature in fully epitaxial Co/MgO/Co magnetic tunnel junctions with bcc Co(001) electrodes. *Appl. Phys. Lett.* **89**, 042505 (2006).
40. Saygun, T., Bylin, J., Hammar, H. & Fransson, J. Voltage-induced switching dynamics of a coupled spin pair in a molecular junction. *Nano Lett.* **16**, 2824–2829 (2016).
41. Bowen, M. et al. Observation of Fowler–Nordheim hole tunneling across an electron tunnel junction due to total symmetry filtering. *Phys. Rev. B* **73**, 140408 (2006). (R).
42. Matsumoto, R. et al. Spin-dependent tunneling in epitaxial Fe/Cr/MgO/Fe magnetic tunnel junctions with an ultrathin Cr(001) spacer layer. *Phys. Rev. B* **79**, 174436 (2009).
43. Natterer, F. D. et al. Reading and writing single-atom magnets. *Nature* **543**, 226–228 (2017).
44. Muenks, M., Jacobson, P., Ternes, M. & Kern, K. Correlation-driven transport asymmetries through coupled spins in a tunnel junction. *Nat. Commun.* **8**, 14119 (2017).
45. Ormaza, M. et al. Efficient Spin-Flip Excitation of a Nickelocene Molecule. *Nano Lett.* **17**, 1877–1882 (2017).
46. Loth, S. et al. Controlling the state of quantum spins with electric currents. *Nat. Phys.* **6**, 340–344 (2010).
47. Hermenau, J. et al. A gateway towards non-collinear spin processing using three-atom magnets with strong substrate coupling. *Nat. Commun.* **8**, 642–650 (2017).
48. Moreno-Pineda, E., Godfrin, C., Balestro, F., Wernsdorfer, W. & Ruben, M. Molecular spin qubits for quantum algorithms. *Chem. Soc. Rev.* **47**, 501–513 (2018).
49. Casola, F., van der Sar, T. & Yacoby, A. Probing condensed matter physics with magnetometry based on nitrogen-vacancy centres in diamond. *Nat. Rev. Mater.* **3**, 17088–17100 (2018).
50. Studniarek, M. et al. Probing a Device's Active Atoms. *Adv. Mater.* **29**, 1606578 (2017).
51. Kim, D. J. et al. Control of defect-mediated tunneling barrier heights in ultrathin MgO films. *Appl. Phys. Lett.* **97**, 263502 (2010).
52. Bardou, F. Rare events in quantum tunneling. *Europhys. Lett. EPL* **39**, 239–244 (1997).
53. Halisdemir, U. et al. Oxygen-vacancy driven tunnelling spintronics across MgO. in *Proc. SPIE Nanoscience + Engineering* Vol. 9931 (eds Drouhin, H.-J., Wegrowe, J.-E. & Razeghi, M.) 99310H (2016).
54. Kent, A. D. & Worledge, D. C. A new spin on magnetic memories. *Nat. Nanotechnol.* **10**, 187–191 (2015).
55. Romera, M. et al. Vowel recognition with four coupled spin-torque nanoo oscillators. *Nature* **563**, 230–234 (2018).
56. Tiusan, C. et al. Spin tunnelling phenomena in single-crystal magnetic tunnel junction systems. *J. Phys. Condens. Matter* **19**, 165201 (2007).
57. Bowen, M. *Experimental Insights into Spin-Polarized Solid State Tunneling*. PhD thesis, Univ. de Paris XI (2003).
58. Serri, M. et al. High-temperature antiferromagnetism in molecular semiconductor thin films and nanostructures. *Nat. Commun.* **5**, 3079–3087 (2014).
59. Barraud, C. et al. Unidirectional spin-dependent molecule-ferromagnet hybridized states anisotropy in cobalt phthalocyanine based magnetic tunnel junctions. *Phys. Rev. Lett.* **114**, 206603 (2015).
60. Barraud, C. et al. Phthalocyanine based molecular spintronic devices. *Dalton Trans* **45**, 16694–16699 (2016).
61. Chung, S.-W. et al. 4Gbit density STT-MRAM using perpendicular MTJ realized with compact cell structure. in *Proc. 2016 IEEE International Electron Devices Meeting (IEDM)* 27. 1.1–27.1.4 (2016).
62. Watanabe, K., Jinnai, B., Fukami, S., Sato, H. & Ohno, H. Shape anisotropy revisited in single-digit nanometer magnetic tunnel junctions. *Nat. Commun.* **9**, 663–668 (2018).
63. Josefsson, M. et al. A quantum-dot heat engine operating close to the thermodynamic efficiency limits. *Nat. Nanotechnol.* **13**, 920–924 (2018).
64. Heinrich, B. W., Braun, L., Pascual, J. I. & Franke, K. J. Protection of excited spin states by a superconducting energy gap. *Nat. Phys.* **9**, 765–768 (2013).
65. Bernos, J. et al. Impact of electron-electron interactions induced by disorder at interfaces on spin-dependent tunneling in Co-Fe-B/MgO/Co-Fe-B magnetic tunnel junctions. *Phys. Rev. B* **82**, 060405(R) (2010).
66. Hayakawa, J., Ikeda, S., Lee, Y. M., Matsukura, F. & Ohno, H. Effect of high annealing temperature on giant tunnel magnetoresistance ratio of CoFeB/MgO/CoFeB magnetic tunnel junctions. *Appl. Phys. Lett.* **89**, 232510 (2006).
67. Halley, D. et al. Electrical switching in Fe/Cr/MgO/Fe magnetic tunnel junctions. *Appl. Phys. Lett.* **92**, 212115 (2008).
68. Kresse, G. & Furthmüller, J. Efficient iterative schemes for ab initio total-energy calculations using a plane-wave basis set. *Phys. Rev. B* **54**, 11169–11186 (1996).
69. Kresse, G. & Joubert, D. From ultrasoft pseudopotentials to the projector augmented-wave method. *Phys. Rev. B* **59**, 1758–1775 (1999).
70. Perdew, J. P., Burke, K. & Ernzerhof, M. Generalized gradient approximation made simple. *Phys. Rev. Lett.* **77**, 3865–3868 (1996).

Acknowledgements

We are grateful to H. Thierschmann, K. McKenna and J. Blumberger for useful discussions, and to Y. Henry for carefully reading our manuscript. Devices were synthesized at the STNano technological platform. We acknowledge financial support from the Institut Carnot MICA (project 'Spinterface'), from the ANR (ANR-09-JCJC-0137, ANR-14-CE26-0009-01), the Labex NIE "Symmix" (ANR-11-LABX-0058 NIE) and Vetenskapsrådet. This work was performed using HPC resources from the Strasbourg Mesocenter and from the GENCI-CINES Grant 2016-gem1100. Open access funding provided by Uppsala University.

Author contributions

M.B., E.B. and S.B. conceived the initial experiment. M.H. grew the sample stack. E.U., F.S., K.K. and J.A. implemented technological processing to make MTJs. E.U., F.S. and K.K. performed magnetotransport measurements. M.B., K.K., S.B., D.L., E.B., M.A. and W.W. analyzed magnetotransport results. B.V. and D.S. performed auxiliary measurements. J.F. designed the analytical models with input from M.B. K.K. applied the analytical models, with input from M.B. and J.F. B.T.

and M.A. implemented DFT calculations with input from M.B. M.B., K.K. and B.T. prepared the manuscript. All authors commented on the manuscript.

Additional information

Supplementary information accompanies this paper at <https://doi.org/10.1038/s42005-019-0207-8>.

Competing interests: The authors declare no competing interests.

Reprints and permission information is available online at <http://npg.nature.com/reprintsandpermissions/>

Publisher's note Springer Nature remains neutral with regard to jurisdictional claims in published maps and institutional affiliations.



Open Access This article is licensed under a Creative Commons Attribution 4.0 International License, which permits use, sharing, adaptation, distribution and reproduction in any medium or format, as long as you give appropriate credit to the original author(s) and the source, provide a link to the Creative Commons license, and indicate if changes were made. The images or other third party material in this article are included in the article's Creative Commons license, unless indicated otherwise in a credit line to the material. If material is not included in the article's Creative Commons license and your intended use is not permitted by statutory regulation or exceeds the permitted use, you will need to obtain permission directly from the copyright holder. To view a copy of this license, visit <http://creativecommons.org/licenses/by/4.0/>.

© The Author(s) 2019